LAWRENCE
LIVERMORE
NATIONAL
LABORATORY

Density of Additively-Manufactured, 316L SS Parts Using Laser Powder-Bed Fusion at Powers Up to 400W

C. Kamath, B. El-dasher, G. F. Gallegos, W. E. King, A. Sisto

December 23, 2013

Disclaimer

This document was prepared as an account of work sponsored by an agency of the United States government. Neither the United States government nor Lawrence Livermore National Security, LLC, nor any of their employees makes any warranty, expressed or implied, or assumes any legal liability or responsibility for the accuracy, completeness, or usefulness of any information, apparatus, product, or process disclosed, or represents that its use would not infringe privately owned rights. Reference herein to any specific commercial product, process, or service by trade name, trademark, manufacturer, or otherwise does not necessarily constitute or imply its endorsement, recommendation, or favoring by the United States government or Lawrence Livermore National Security, LLC. The views and opinions of authors expressed herein do not necessarily state or reflect those of the United States government or Lawrence Livermore National Security, LLC, and shall not be used for advertising or product endorsement purposes.

This work performed under the auspices of the U.S. Department of Energy by Lawrence Livermore National Laboratory under Contract DE-AC52-07NA27344.

Density of additively-manufactured, 316L SS parts using laser powder-bed fusion at powers up to 400W

Chandrika Kamath[1], Bassem El-dasher[1], Gilbert F. Gallegos[1], Wayne E. King[1], and Aaron Sisto[2]

[1] Lawrence Livermore National Laboratory, Livermore, CA 94551
[2] Stanford University, Stanford, CA 94305

Abstract

Selective laser melting is a powder-based, additive-manufacturing process where a three-dimensional part is produced, layer by layer, by using a high-energy laser beam to fuse the metallic powder particles. A particular challenge in this process is the selection of appropriate process parameters that result in parts with desired properties. In this study, we describe an approach to selecting parameters for high density (>99%) parts using 316L stainless steel. Though there has been significant success in achieving near-full density for 316L parts, this work has been limited to laser powers <225W. We discuss how we can exploit prior knowledge, design of computational experiments using a simple model of laser melting, and single-track experiments to determine the process parameters for use at laser powers up to 400W. Our results show that, at higher power values, there is a large range of scan speeds over which the relative density remains >99%, with the density reducing rapidly at high speeds due to insufficient melting, and less rapidly at low speeds due to the effect of voids created as the process enters keyhole mode.

Keywords: 316L stainless steel, keyhole-mode laser melting, additive manufacturing, powder-bed fusion, selective laser melting, direct metal laser sintering

1   Introduction

Laser powder-bed fusion additive manufacturing (AM) is a method by which metal parts can be produced layer by layer. The design freedom afforded by this process is accompanied by complexity. For example, Yadroitsev (2009) indicates that there are more than 130 parameters that could affect the final quality of the material that is being produced. These include laser power, scan speed, scan-line spacing (hatching), powder layer thickness, scanning strategy, atmosphere, and powder bed temperature. Ranking the parameters in order of importance is critical to limiting the scope of design of experiments (DOE) studies that are a common approach to identifying sets of parameters that optimize material properties such as density. An example of the use of DOE methods to rank parameters is given in the main effects analysis of Delgado et al. (2012). It is not unusual for DOEs to include hundreds of samples to reach an optimal set of process parameters, making such investigations time consuming and expensive.

Additively manufactured 316L stainless steel has been studied in a number of previous investigations. It is one of the materials where there has been significant success in achieving near full density. However, as the studies in Table 1 indicate, this previous work has been limited to laser

Power range (W)	Speed range (mm/s)	Beam size (μm)	Layer thickness (μm)	Hatch spacing (μm)	Highest relative density	Reference
85-105	300	$\Phi(99\%)$=200	20-60	112-125	98.8-99.2	Yasa et al. (2009),
104	300-800	200	30	130	99.3-99.5	Spierings and Levy (2009)
100	300	$\Phi(99\%)$=180	30	81-126	98.4-98.9%	Yasa et al. (2010)
50	120	70	40	120	99+%	Yadroitsev and Smurov (2010)
105	380	$\Phi(99\%)$=200	20-40	125	99.25-99.8	Kruth et al. (2010a)
100	175-380	$\Phi(99\%)$=180	60	126	95.8-98.8	Kruth et al. (2010b)
105	380	$\Phi(99\%)$=200	N/A	125	99.2	Yasa et al. (2011)
100	300	$\Phi(99\%)$=180	30	112-125	98.8-99.2	Yasa (2011)
50	100-300	26-48	50	80	96.72-99.93	Liu et al. (2011))
87	150	180	75	130	82	Dadbakhsh et al. (2012)
175	80-200	N/A	100	40-60	80.4-98.5	Laohaprapanon et al. (2012)

Table 1: Prior work on the density of additively manufactured 316L stainless steel parts. N/A indicates that the parameters values are not available. Not all authors include the definition of the beam spot size used in their work; when they do, the definition has been noted in the table.

powers <225W. Recently, metal additive-manufacturing machines have become available with powers up to 1000W, as described in the work of Niendorf et al. (2013) on the microstructure and mechanical properties of 316L stainless steel at powers of 400W and 1000W.

But, this increasing laser power is accompanied with the increasing likelihood that the mechanism for melting of the powder in the powder bed and the fusion of that molten material to underlying material could transition from being controlled by thermal conduction to being controlled by the so-called keyhole mode melting as described in Rai et al. (2007). In keyhole-mode laser melting, the power density of the laser beam is sufficient to cause evaporation of the metal and formation of plasma. Metal evaporation causes the development of a vapor cavity that enhances the laser absorption. This enables the laser beam to drill to a far deeper depth than is possible in conduction-controlled mode. Collapse of the cavity can leave voids in the wake of the laser beam, as shown in Madison and Aagesen (2012).

Therefore, reaching full density requires balancing laser power, scan speed, beam size, and layer thickness to ensure on one hand that the layer fully melts and on the other hand that the melting does not result in development of a large amount of voids due to the keyhole mode mechanism. Thus, one might expect that using higher powers, with the accompanying higher laser speeds, might narrow the processing window to achieve near full density. However, there is evidence (see Buchbinder et al. (2011)), in experiments on aluminum alloys at 300, 500, 700, and 1000W, that increasing laser power broadens the processing window.

In this study, we investigate the effect of process parameters on density of 316L stainless steel for laser powers up to 400W. This paper is organized as follows. First, we describe how we use data mining techniques to gain insights into simple experiments and simulations that model the process of laser melting. By combining these results with prior information, we are able to streamline the

process of parameter optimization, and identify parameters likely to result in high-density parts. Next, we describe our experimental approach, including the process used to determine the density of simple square pillars that were built using the parameters determined earlier. We then present the results of our experiments, along with the insights gained in this study and conclude with a brief summary of our work.

2 Selecting the experimental parameters

Our experiments were conducted using a Concept Laser M2 laser powder-bed fusion machine with a maximum power of 400W and a spot size, D4σ, of 54μm. Since much of the work in identifying optimal process parameters for high density for 316L stainless steel has been done on machines with a lower power of 100W (see Table 1 in Section 1), a major challenge was to identify the appropriate parameters for use with these higher-power machines. To achieve our desired goal of identifying process parameters that would result in high density (>99%) parts in relatively few iterations, we exploited all the information available to us, including prior knowledge, simple simulations, simple single-track experiments, and data analysis techniques to help guide the selection of these parameters.

2.1 Exploiting prior knowledge

Our work was influenced to a large extent by earlier work done by Kruth et al. (2010a) and Yasa (2011). In her thesis, Yasa (2011) indicated that using 100W lasers with a spot size $\Phi(99\%)$ of 180 μm, high density parts (in this case, small square pillars of AISI 316L material), with good surface quality, could be obtained using a scan speed of 300mm/s, layer thickness of 30 μm, and scan spacing factor of 0.62. The scan spacing, which is the distance between consecutive scan tracks, was set to the scan spacing factor times the spot size. Given the spot size of the machine and the setting of the scan spacing factor, this resulted in a scan spacing of 112 μm. The powder size for the AISI 316L was D(v,0.5)= 42 μm, indicating that 50% of the total volume of powder is composed of particles larger than 42 μm in diameter. In Kruth et al. (2010a), the optimal parameters for high density parts for AISI 316L stainless steel material at the slightly higher laser power of 105W and a slightly larger spot diameter $\Phi(99\%)$ of 200 μm were found to be a scan speed of 380mm/s and a scan spacing of 125 μm. Since the spot diameter of our machine (equivalent to $\Phi(99\%) = 81$ μm) is much smaller than the one used in this prior work, we could not directly use these optimal process parameters to build high density parts even at 100-105W. However, this prior work did provide an initial estimate of the optimal parameters at low power settings.

Additional details in Yasa's thesis (Yasa (2011), pp. 147) indicated that, for a fixed power and scan speed, the density improved as the layer thickness was reduced, with a layer thickness of 30 μm resulting in the highest density. For a fixed layer thickness, as the scan speed was increased from 100 to 200 mm/s, the relative density dropped from 98-99% to 96-98%, falling more rapidly to a range of 85-95% at 400mm/s. Based on this, we selected a layer thickness of 30 μm for our experiments as this setting had the smallest drop in density with increasing scan speeds making it the least sensitive to changes in the scan speed.

In addition to these prior experiments at low power (100W) that explicitly provided optimal parameters for high density, our understanding of the laser melting process also suggested that for a given power, as we increased the scan speed, the density would decrease as there was less melting of the powder. Also, for a given power setting, low speeds would result in very deep melt pools, with

possible formation of voids due to keyhole-mode laser melting, resulting in possibly lower density. Therefore, to identify the optimal process parameters at higher values of the laser power, we had to select a scan speed that would not be too low nor too high. This was difficult as we did not know how the speed should be varied as the laser power was increased from 100W to 400W. In addition, for a specific power setting, it was unclear if the range of speeds over which high density parts were obtained was broad, making it easy to identify an optimal value, or relatively narrow, which would make the identification of optimal parameters challenging.

2.2 Use of simple simulations

To obtain some insights into what we might expect at higher power values over a range of scan speeds, we considered a simple, computationally-inexpensive simulation that would allow us to bracket the parameters for a design of (physical) experiments investigation into optimal parameters for high-density parts. Since the laser spot size is considered to be an important parameter, the Eagar and Tsai solution (Eagar and Tsai, 1983) was used to compute the temperature distribution of the surface of the melt pool and the longitudinal melt-pool cross-section as a function of AM parameters including laser beam energy, speed, and spot size. From this, we could calculate the melt pool length, width, depth, and area. The Eagar-Tsai model is a relatively simple model that considers a Gaussian beam on a flat plate to describe conduction-mode laser melting. The presence of powder is not considered. This simplicity of the model made it computationally inexpensive; as a result, it was possible to sample the input parameter space of the simulations rather densely. However, since it does not model the powder, the results were approximate and used mainly as an initial estimate of laser power and speed values to use in our experiments.

To understand how the melt-pool characteristics, including the length, width, and depth, would change with power and scan speed, we conducted a full fractional design of computer experiments (Oehlert (2000) and Fang et al. (2005)) using the Eagar-Tsai model. There were four input parameters: laser power, scan speed, spot size, and laser absorptivity. We varied the speed from 50mm/s to 2250mm/s with 10 levels, the power from 50W to 400W using 7 levels, the spot size (D4σ) from 50 μm to 68 μm using 3 levels, and the laser absorptivity from 0.3 to 0.5 using 2 levels. This resulted in 462 parameter combinations that were input to our simulation.

The range of values for each variable was selected as follows. Our CL20 machine had a peak power of 400W, which determined the upper bound on the power. The lower limit on the speed was set to ensure sufficient melting at the low power values such that the melt-pool depth would be at least 30μm (the layer thickness selected for our experiments). The upper limit on the speed was estimated at a value that would likely result in a relatively shallow melt pool at the high power value. The lower and upper limits on the spot size were obtained from measurements of the spot size on our machine at focus offsets of 0mm and 1mm. By varying the spot size and the absorptivity, we were able to account for possible variations in these parameters over time or build conditions as we built the parts.

The outputs of the 462 simulations were analyzed in two ways. First, we considered the depth of the melt pool. Since we had decided on a layer thickness of 30 μm, we identified the simulations that resulted in depths ranging from 60 μm to 120 μm as possible candidates. This essentially removed the cases where there was insufficient melting or the melt pools were too deep. Our use of a simple rule to narrow down the cases we wanted to consider further is justifiable as the Eagar-Tsai model is a simple approximation to what we would see in an actual experiment. We then focused on simulations that had laser power values at least 150W as we were interested mainly

4

in the higher power settings. The resulting subset of 150 simulations was then used to identify possible parameters settings for physical experiments that would likely result in high-density parts.

We then considered the melt pool widths in this subset of 150 simulations. This ranged from 125 μm to 240 μm, with two-thirds of the simulations (101 simulations) having widths in the range of 125 μm to 175 μm. This provided us an estimate of the trace widths (that is, the width of a single track) to use in the physical experiments (see Section 3).

Figure 1 shows a parallel-coordinate plot (Inselberg (2009)) that summarizes the inputs to the 462 simulations and the corresponding melt-pool depths. Parallel coordinate plots are a way of displaying high-dimensional, mult-variate data. First, the four inputs and the depth are individually scaled to lie between 0 and 4.0, enabling them to be displayed on a single plot. The x-axis displays the four inputs and the output. Each simulation is a poly-line that connects its scaled values of the four inputs and the scaled width. The simulations have been grouped into three groups, depending on whether the melt-pool depth is less than 60μm (247 cases), greater than 120μm (40 cases), or in between (175 cases). The poly-line corresponding to each simulation is assigned a unique color based on the depth. Of the 175 cases in the third group (in blue in the plot), 150 have power values at least 150W.

The parallel coordinate plot provides some insights into the range of process parameters we should consider further. First, we observe that deep melt pools (in purple in panel (a) or in panel (d)) result when the speed is very low, and the power is typically very high (though it can be moderate as well). Very shallow melt-pools (in blue in panel (a) or in panel (b)) result when the speed is relatively high and the power is relatively low (though it can be moderate as well). This indicates that speed is likely to be an important variable in determining the melt-pool depth, with power being a close second. The other two variables - beam spot size and absorptivity - have the three colors spanning the full range of low to high values, indicating that they are relatively less important in determining the depth.

2.3   Feature selection

Next, we used the 462 Eagar-Tsai simulations to identify the important input parameters for the melt pool characteristics. Prior work of Yasa (2011) had indicated that, for the parameter ranges considered in their experiments, the laser power, scan speed, layer thickness, and scan spacing were the most important process parameters in generating high-density parts. In the absence of a reasonable amount of experimental data relating various process parameters to the density of a part, we used the Eagar-Tsai simulations themselves to identity which of the four inputs - laser power, scan speed, spot size, and absorptivity - were most important in determining the characteristics of melt-pool depth, length, and width. We accomplished this using feature selection techniques from data mining (Kamath (2009)). These techniques essentially rank each input variable using a metric that indicates how relevant the input is to the output. For example, the Pearson correlation coefficient between two vectors, X and Y, defined as

$$\frac{Cov(X,Y)}{\sigma_X \sigma_Y}$$

where $Cov(X,Y)$, the covariance between the two vectors, is a measure of how correlated the input X is to the output Y. If an input parameter is not correlated to any of the melt-pool characteristics, then it does not make sense to vary its value in designing the physical experiments. In our work, we used an ensemble of feature selection methods described in Sisto and Kamath (2013) to rank the
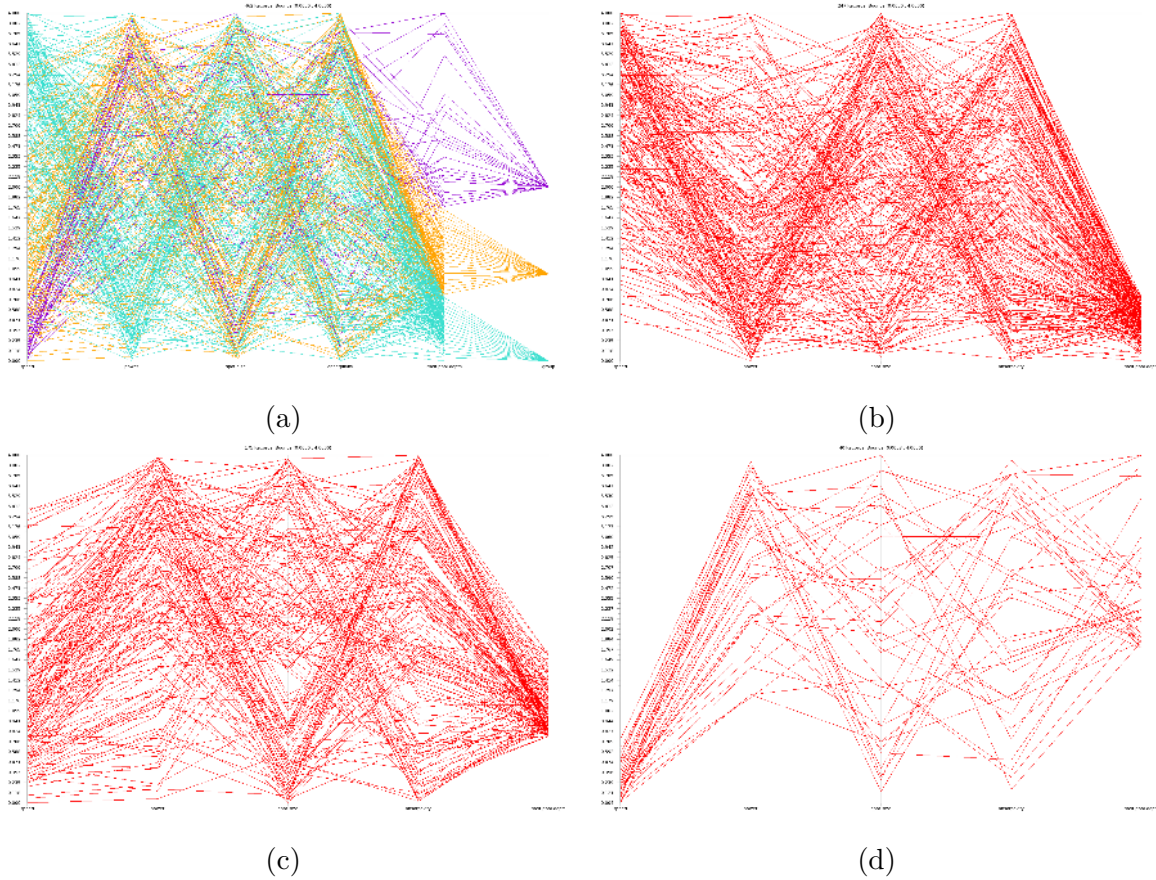
5

(a)

(b)

(c)

(d)

Figure 1: A parallel-coordinate plot showing the values used in the 462 simulations and the corresponding melt-pool depths. The four inputs and the output are shown on the x-axis in order: speed, power, spot size, absorptivity, and melt-pool depth. Each simulation input, consisting of 4 values, is a poly-line in the plot connecting the values of the inputs and output for that simulation. Each of the four inputs and the output have been scaled to lie between 0 and 4 so they can be displayed on a single plot. The simulations have been grouped into three: melt-pool depth less than 60 µm (panel (b)), between 60 µm and 120 µm (panel (c)), and greater than 120 µm (panel (d)). Panel (a) shows the three groups combined in one plot with each simulation assigned a color based on one of these three groups. The group is the last variable shown on the x-axis in panel (a).

relevance of the four input parameters in the Eagar-Tsai model. This ensemble approach combines the results of several feature selection methods to give a more robust result. We also included an additional noise parameter whose rank would indicate if any of the inputs were irrelevant to the melt-pool characteristics, as these input parameters would be ranked lower than the noise variable.

The results of feature selection using the 462 simulation are summarized in Table 2. This indicates the rank of each of the four input parameters, and the noise variable, for each of the three outputs - the melt-pool width, length, and depth. A higher number indicates a higher rank. For all three outputs, the two highly-ranked inputs were clearly identifiable, while the metrics for the lower-ranked ones were often very close or identical, and much lower than the ones for the top ranked parameters. The relative ranking of the three lowest-ranked inputs is therefore not significant. Further, the ranking reflects the range of the input parameters used in generating the data, and would likely change if different ranges were used.

The results in Table 2 indicate that for the melt-pool width and depth, the scan speed and laser power are the most important inputs, while for the melt-pool length, the laser power and absorptivity are the most important inputs. Note that a similar result is observed for the melt-pool depth using the parallel coordinate plot in Figure 1. Based on this, since the melt-pool width and the depth are the main characteristics of interest in determining the processing parameters, we decided to focus on varying the laser power and the scan speed in our initial set of experiments.

	Speed	Power	Beam size	Absorptivity	Noise
Melt-pool width	5	4	1	2	3
Melt-pool length	2	5	1	4	3
Melt-pool depth	5	4	1	2	3

Table 2: Rank order of the input parameters to the Eagar-Tsai mode: a higher rank indicates a more relevant input. The values of the metrics used in the ranking is typically the same or very close for the three lowest ranked inputs.

2.4 Use of single track experiments

Once we had identified possible ranges of power and speed that would result in sufficiently deep melt pools using the Eagar-Tsai model (see Section 2.2), we selected a small set of power and speed values for use in single-track experiments, as described in Yadroitsev et al. (2010). For each power value selected, we estimated values of speeds such that at low speeds, we obtained deep melt pools, while at higher speeds, there was just sufficient melting so the melted powder adhered to the substrate.

We used a 40mm x 40mm build plate (see Figure 2), with a tilt so that the layer thickness was 0 at the left and 200 μm at the right. Fourteen tracks were created using different power and speed settings as shown in Table 3, where track 1 is the track at the top of the Figure 2. The build plate was then sliced at different values along the x-axis so the melt-pool structure at different layer thicknesses could be studied. Table 3 also includes the melt-pool height (above substrate), depth (below substrate), and width (at substrate) for the 14 tracks. These results are obtained at a layer thickness of 30 μm corresponding to a cut 6mm from the left edge of the plate. The images of the melt-pool corresponding to four sample tracks at 300W are shown in Figures 3 and 4.

We make the following observations on the results from the single track experiments. First, as expected, increasing the laser power or reducing the scan speed results in greater melting of the powder and the substrate. However, the relationship appears to be non-linear, making it difficult to estimate the optimal speed at 400W if we know the optimal speed at, say, 100W. Second, for a given power and scan speed, as the layer thickness increases, the melting is reduced, which is also expected. This is clearly seen in the last three tracks on the plate, where at 150W, more of the track appears on the plate as the speed is reduced from 1200 mm/s to 800mm/s to 500mm/s. The third track from the bottom (at 1200mm/s) does not result in any melting at higher layer thickness, unlike the last track (at 500mm/s), which creates a continuous track until nearly the edge of the plate. In contrast, the tracks at the top of the plate, which are at higher powers, run the entire length of the plate.
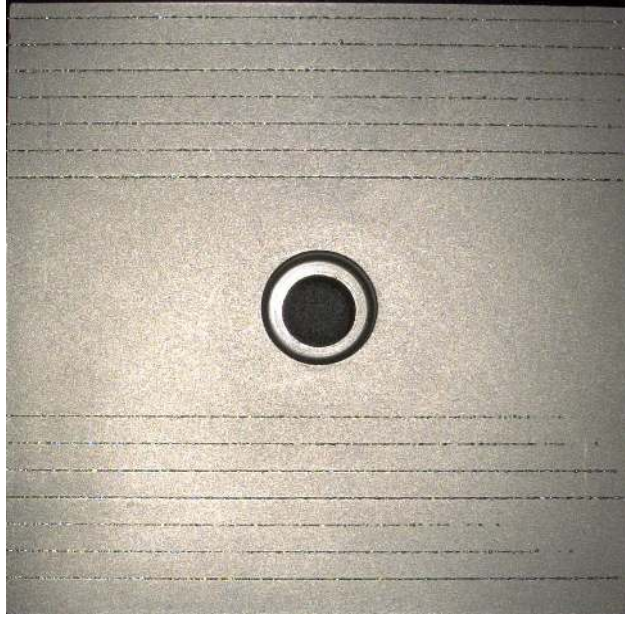
Figure 2: The 40mm × 40mm tilted build plate with the 14 tracks, each generated using a different value of laser power and scan speed, as listed in Table 3, where track 1 corresponds to the track at the top of the plate. In the tilted plate experiment, the layer thickness starts at near zero at the left edge, increasing linearly to 200 μm at the right edge.

Track number	Power (W)	Speed (mm/s)	Width (μm)	Height (μm)	Depth (μm)
1	400	1800	112	32	105
2	400	1500	103	79	119
3	400	1200	83	28	182
4	300	1800	94	57	65
5	300	1500	83	35	94
6	300	1200	111	76	114
7	300	800	118	54	175
8	200	1500	84	26	57
9	200	1200	104	45	68
10	200	800	123	24	116
11	200	500	121	61	195
12	150	1200	79	21	30
13	150	800	109	44	67
14	150	500	115	40	120

Table 3: The melt-pool width, height, and depth for the 14 tracks, along with the laser power and scan speed settings. Track 1 corresponds to the track at the top of the plate in Figure 2.

Finally, we observe that the depth of the melt pool can be quite large, with a maximum of 195 μm for track 11, which is several times the layer thickness at 30 μm. On one hand, we want the depth to be sufficient so that the powder that has melted adheres to the previous layer. However, too deep a melt pool could indicate keyhole-mode melting that could result in voids, thus lowering the density of the part. It would also imply that we were either using more power than necessary, thus heating both the part and powder which could affect the microstructure and mechanical properties of the part, or using a lower speed than necessary, thus increasing the build time.

(a)   (b)
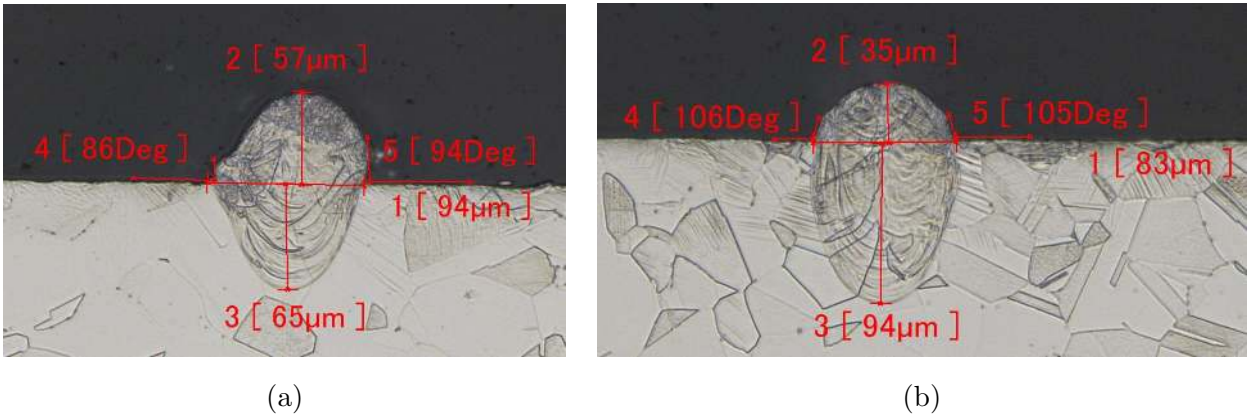
Figure 3: The melt-pool width, height, and depth for (a) track 4 at 300 W and 1800 mm/s and (b) track 5 at 300W and 1500 mm/s.
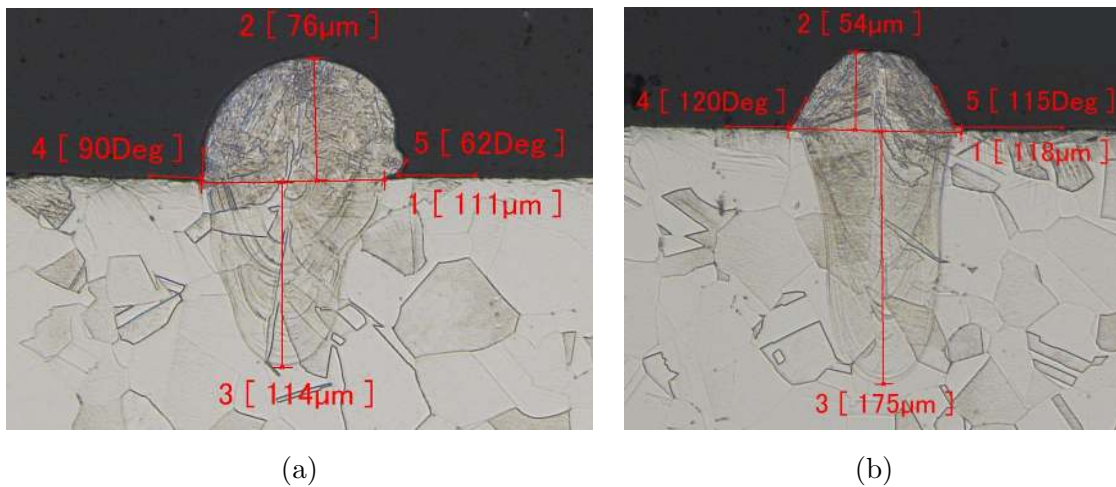

(a)   (b)

Figure 4: The melt-pool width, height, and depth for (a) track 6 at 300 W and 1200 mm/s and (b) track 7 at 300W and 800 mm/s.

2.5 Selecting process parameters for high-density parts

Next, to identify the power and speed values that would result in high (>99%) density parts, we built small pillars, each at different power-speed values, and evaluated their density. Following earlier work by Yasa (2011), our pillars were 10mm × 10mm × 7mm. These were placed 10mm apart on the build plate, as shown in Figure 5.

The power and speed values for each pillar were selected based on the analysis of the Eagar-
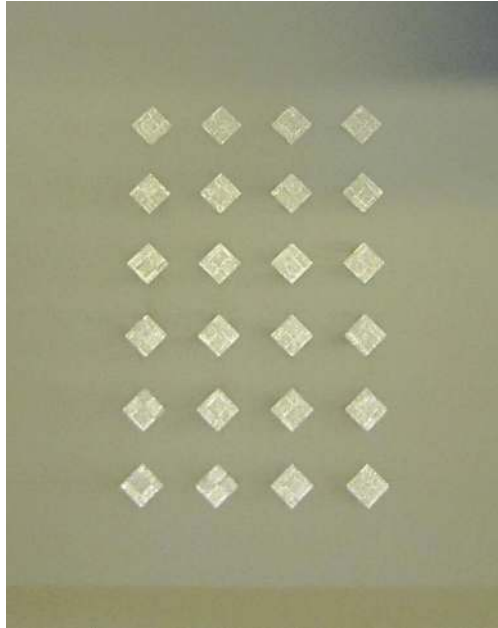
Figure 5: An image of the 24 pillars after they have been built, but before they have been removed from the powder bed. Each row corresponds to one power setting, with the top row at the lowest setting of 150W and the bottom row at the highest setting of 400W.

Tsai simulations, the single track experiments, and earlier work at lower power. A particular challenge was to determine the range of speeds to use for each power setting, given that extensive experimentation was not desirable. The higher end of this range was bounded by the requirement that we wanted the powder to melt and the melt-pool depth to be sufficient so that the new layer adhered to the previous one. We had also observed in the single-track experiments that deeper melt pools tended to be "cleaner", exhibiting left/right symmetry, with the cross-section of the melted powder in the form of a semi-circle. This led us to hypothesize that power and speed settings that resulted in melt pools with depths that were 2-3 times the layer thickness might be in the appropriate range for high-density parts. The re-melting of previous layers that would occur in a deep melt pool might also result in increased density as observed in Yasa's thesis (Yasa (2011), pp. 187), where explicit re-melting after each layer significantly reduced porosity.

Based on this, we carefully selected an initial set of 24 power-speed combinations (see Figure 8) to create our first set of pillars. We used six different power values, with four speeds for each. Our intent was to obtain the range of parameters that would result in high-density parts by building and analyzing a relatively small number of pillars.

3   Experimental procedure

Our experiments to create high-density 316L stainless steel pillars using additive manufacturing were carried out using a Concept Laser M2 powder-bed fusion additive manufacturing machine under Argon atmosphere. The M2 has a 400W fiber laser with a laser spot size, $D4\sigma = 54\ \mu m$. As mentioned earlier, we explored a range of laser power and scan speed options, while keeping the rest of the process parameters constant. Specifically, we used the island scanning pattern from Yasa (2011) with 5mm x 5mm islands (see Figure 6, panel (a)). The size of the pillars (10mm x 10mm)

(a)   (b)   (c)
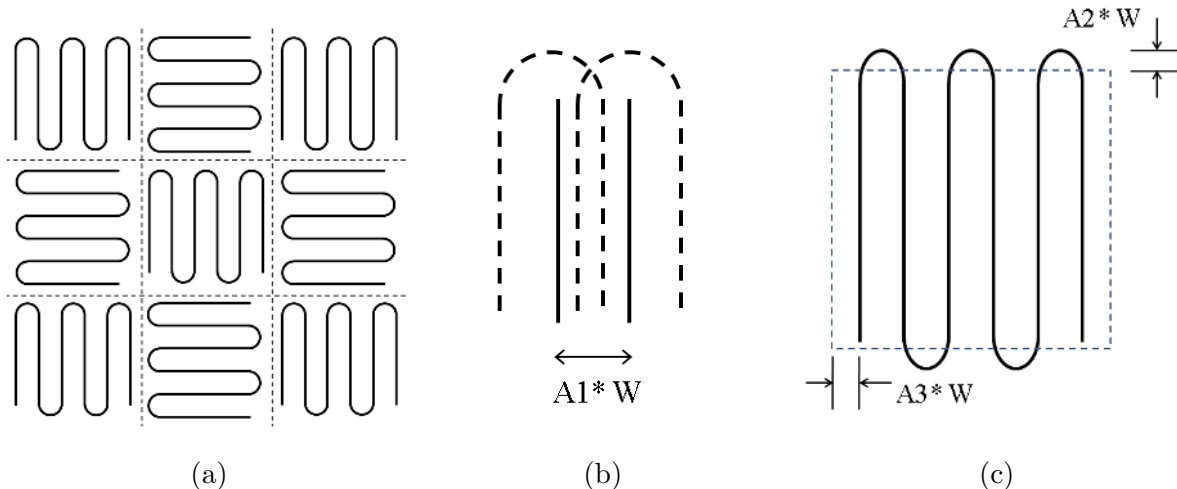
Figure 6: (a) The island scanning pattern that covers each layer with small islands, with the powder on each island area melted by traversing a serpentine path. The paths in adjacent islands are orthogonal to each other. (b) The overlap, A1, between scan lines as a fraction of the track width, W; the solid line is the path of the laser and the dotted line is the track created by the melt pool. This ensures that there is no space between consecutive scan lines. (c) The elongation, A2, of a scan line in the direction of the scan as a fraction of the track width, W, and the overlap, A3, along the sides of the first and last scan line as a fraction of the track width. A2 and A3 ensure that the islands are connected to each other. The dotted square indicates the boundary of an island.

was chosen to be reasonably larger than the island size to avoid small fragments of islands in layer. We set the track width to 150 μm, which is the default. The analysis of Eagar-Tsai simulations (Section 2.2) suggested that this was an appropriate choice, though the results from the single track experiments (Table 3) indicated that this might be a bit high. The parameters A1 (spacing between scan vectors), A2 (overlap of scan vectors between the islands at the start and end of the vectors), and A3 (overlap of the scan vectors between the islands at the sides of the vectors), were set to 70%, 15%, and 15% of the track width, respectively, as shown in Figure 6, panels (b) and (c). These are the default parameters suggested for the machine; our plan was to start with the default parameters and fine tune them later as necessary. The outside contour of each pillar was built using the default of 200W, 1600mm/s, and the beam compensation (distance between the outside contour and the part) was set to 55 μm. The layer thickness was set to 30 μm.

We used two types of powder in our work - CL20 ES and LPW - with the size distribution shown in Figure 7. By using two different powders, we could determine if powder type had a significant effect on the density of parts.

3.1   Measurement of density

We used two different measurements for the density of the small pillars that were built using additive manufacturing. First, the density of each pillar was obtained using the Archimedes method, as described in Section 3.1.1. However, as Yasa et al. (2010) have observed, the Archimedes method is a general approach for comparing the densities of different samples, but it may not be the best method for measuring density of additively-manufactured parts. This is because the pores formed during the laser melting process may contain some unmelted powder particles, resulting in the density, as measured by the Archimedes method, being different from the real density of a sample.
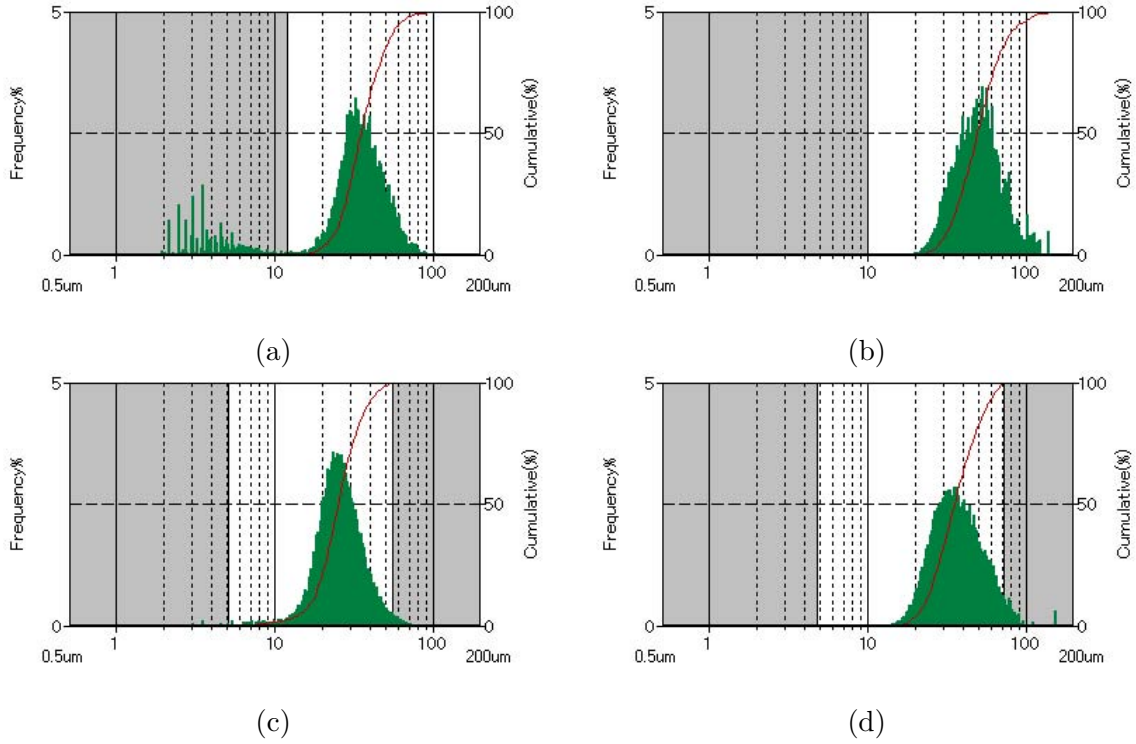
Figure 7: *Distribution of the particle size for the LPW 316L powder (panels (a) and (b)) and the CL20ES powder (panels (c) and (d)). The left column is the distribution by diameter and the right column is the distribution by volume. Note that the scale for the x-axis is logarithmic, green is the distribution, and red is the cumulative distribution.*

Therefore, we also measured the density of a select number of our samples by microscopically measuring the volume fraction of the pores, as described in Section 3.1.2.

3.1.1 Archimedes Method

We measured the density of our sample pillars using the Archimedes method based on the approach suggested in Spierings and Levy (2009). First, all samples were cleaned ultrasonically in three steps: they were washed with Micro, a dilute soap solution; next, they were rinsed in deionized water: and finally, they were rinsed in isopropyl alcohol. Each clean/rinse step was 5 minutes long. The samples were then transferred to labeled bottles and out-gassed in a vacuum oven overnight. No heat was applied.

Next, we recorded the sample weights using a Mettler Toledo XP204 balance equipped with an immersion density kit. The exterior of each sample was then coated with Soft Yucca Optical Wax to seal the porous outer surface and the sample weights recorded again on the Mettler XP 204 balance.

We then used the balance to record immersion density measurements, using a stainless steel sphere for calibration. Three measurements were taken for each sample and averaged to obtain the immersed weight of the sample. From this, the porosity (in percentage) for each pillar was estimated as

$$\frac{((H - S) - (B/7.98))}{(H - S)} * 100$$

where H is the combined volume of the wax-coated sample, S is the volume of the wax, and B is the air weight of the sample. The volume of the wax-coated sample was obtained by dividing the weight of the displaced liquid by its density, where the weight of the displaced liquid is, per the Archimedes' principle, the weight of the wax coated sample in air minus its apparent weight when immersed. The relative density of a sample (in percentage) was (100-porosity).

3.1.2 Measurements using Scanning Electron Microscope

In addition to using the immersion density measurements to estimate of the porosity of each sample, we also used micrographs captured in backscatter mode using an FEI Quanta 200 Scanning Electron Microscope (SEM). Between 21 and 25 micrographs from each specimen were captured at a fixed magnification and working distance such that they yielded a calibrated spatial resolution of $0.61\mu m$, that is, the smallest void recorded could be $0.61\mu m \times 0.61\mu m$.
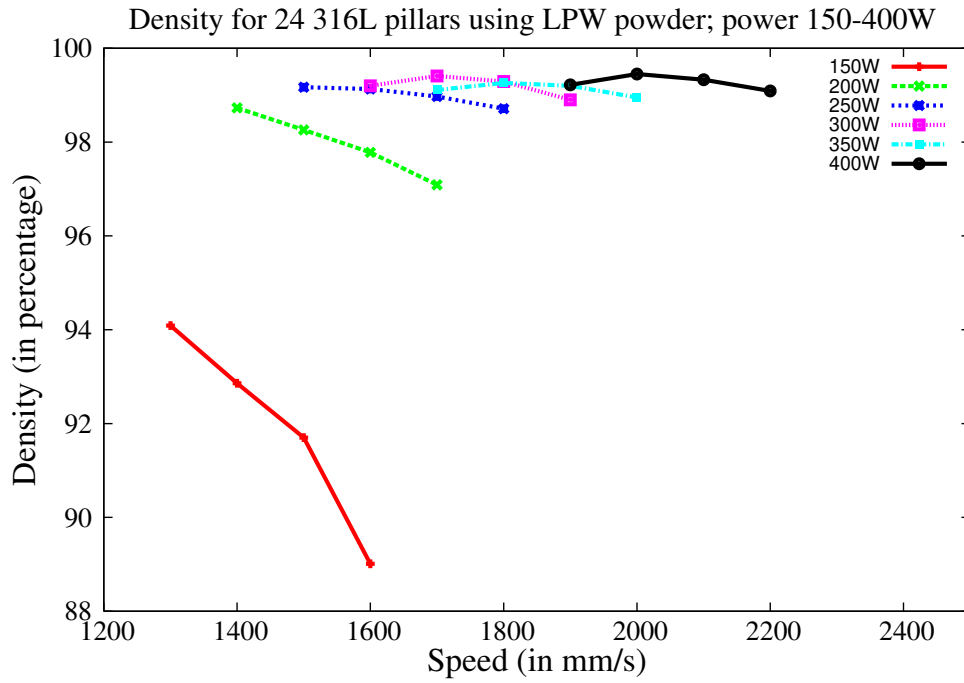
Since voids appear significantly darker than the regular granular microstructure in the backscatter micrographs, thresholding each micrograph into a binary image allowed for the direct calculation of the void area fraction of voids in each micrograph (and subsequently each specimen), which is stereologically equivalent to the volume fraction. This analysis was done using 8 pillars from the first set of 24 pillars built using the LPW powder.The pillars were chosen so that they spanned a range of power values, and included pillars created with different power values, but same speed, as well as different speeds, but same power values.
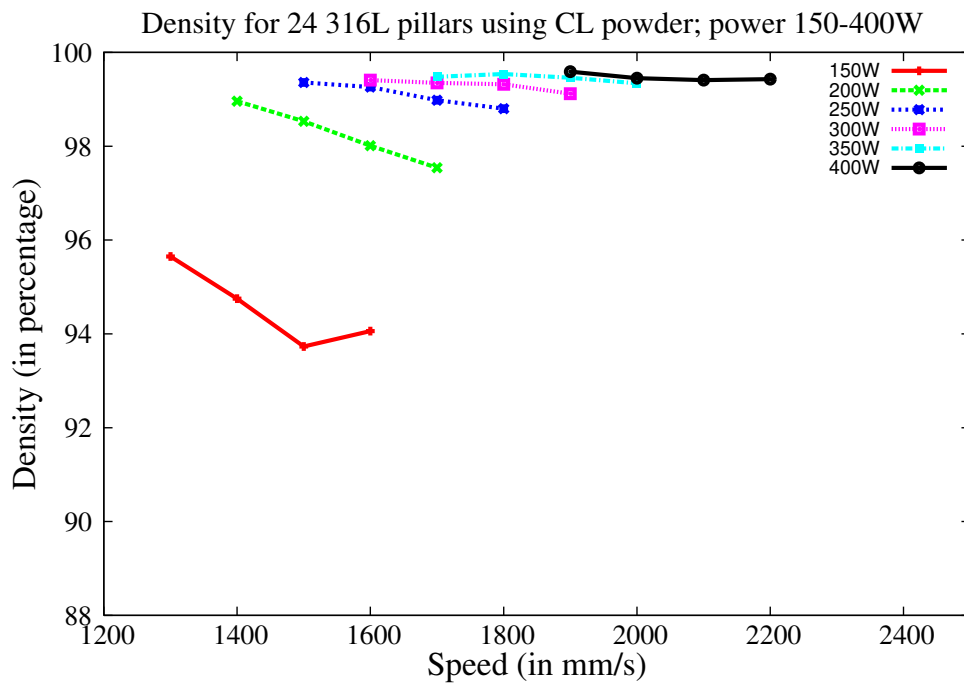
4   Results and discussion

We next present the results of our experiments to identify the power and speed parameters that would result in high-density, metal parts manufactured using an additive process. Our first two sets of 24 pillars were built using the LPW and CL20ES powders, respectively. The density obtained using the Archimedes method is given in Figure 8 for different combinations of laser power and scan speeds. We make several observations on these plots. First, for both powder types, it is possible to obtain high relative density, greater than 99%, at laser power of 250W or higher. For the lower power values, the choice of scan speeds used did not result in a relative density > 99%; however, the plots indicate that high density could be obtained using suitable speeds. Next, we observe that, at lower power values, the density tends to drop off quite quickly as we increase the speed. In contrast, at 400W, the relative density remains nearly constant at 99.5% as the speed is varied from 1900mm/s to 2200mm/s. Finally, we observe that the LPW powder results in lower density at 150W and 200W in comparison with the CL20ES powder; however, this difference diminishes at higher power values.

These plots appear to confirm our expectation that the density will reduce at higher speeds due to insufficient melting. This is observed clearly at the lower power values for both powder types. It also appears, though much less clearly, that the density reduces as we reduce the speed and the process enters the keyhole mode, which could result in voids.

These results prompted us to experiment with a third set of 24 pillars, with the power and speed values chosen to complete the curves generated in Figure 8. For each power value, we selected the speeds so that we had a reasonable number of points on either side of the peak density. This set of 24 pillars was built using CL20ES powder. The combined plot for the relative density for the 48 pillars built using CL20ES powder is shown in Figure 9, where panel (b) excludes the data
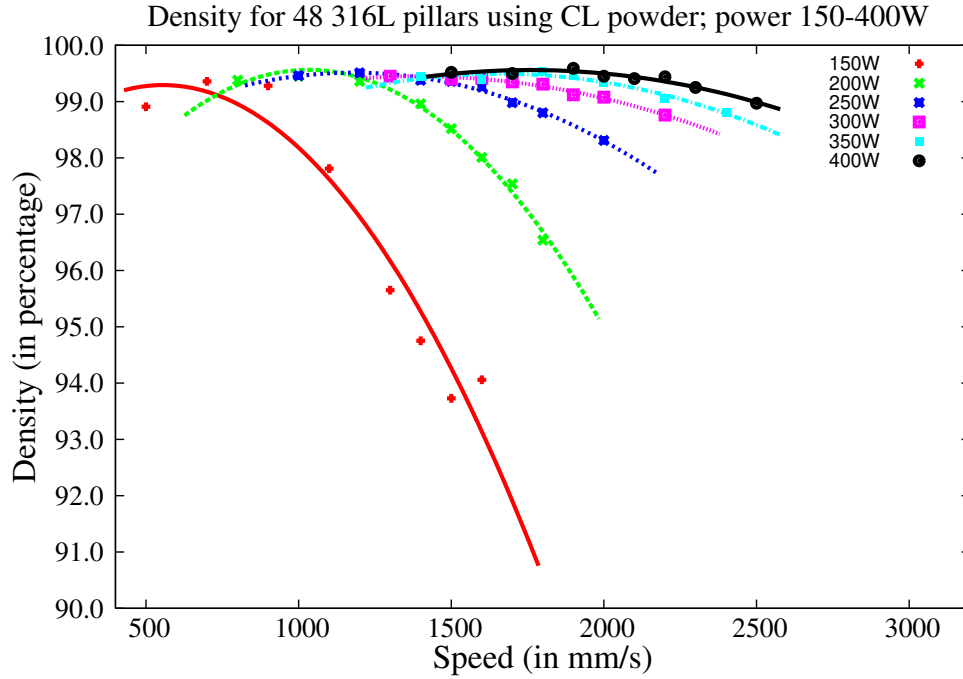
Density for 24 316L pillars using LPW powder; power 150-400W

(a)

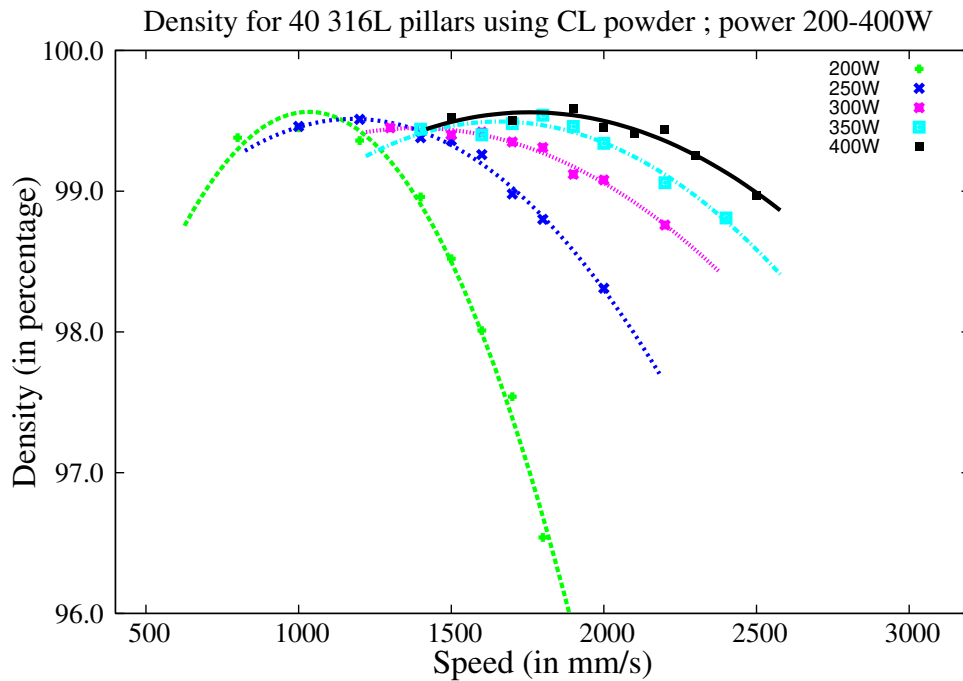Density for 24 316L pillars using CL powder; power 150-400W

(b)

Figure 8: Relative density as a function of laser power and scan speed using (a) LPW powder and (b) CL20ES powder. Both plots use the same range for the y axis for comparison. Density was obtained using the Archimedes method.

(a)

(b)

Figure 9: Relative density as a function of laser power and scan speed using CL20ES powder and additional sample points to complete the curves shown in Figure 8(b). Plot (b) excludes the values for power =150W to illustrate the variation at high density. A quadratic function is fitted to the points for each power value. Density was obtained using the Archimedes method.

Power (W)	Speed (mm/s)	SEM Porosity(%)	Archimedes Porosity (%)	Difference (Archimedes-SEM,%)
200	1600	1.42	2.22	0.8
250	1500	0.48	0.83	0.35
250	1600	0.28	0.87	0.59
250	1800	0.58	1.29	0.71
300	1700	0.14	0.8	0.66
300	1800	0.23	0.59	0.36
300	1900	0.33	1.1	0.77
400	1900	0.19	0.78	0.59

Table 4: The porosity using SEM for a subset of eight pillars built using the LPW powder. The porosity estimated using the Archimedes method is included for comparison..

at 150W to show the variation at higher density clearly. This plot clearly indicates that at low speeds, as we enter the keyhole regime, the density reduces. However, this reduction is not as large as the reduction at higher speeds resulting from insufficient melting of the powder. Further, at higher power, the density remains high over a large range of speeds, while at lower power values, the curves are more peaked, with the density dropping off quickly from its peak value.

Since the density is obtained using the Archimedes method, it prompts the obvious question of the error in the measurement of the density. The immersed weight of each pillar (which is roughly 3.5g) is measured three times and is accurate to the fourth digit after the decimal point. The maximum variation among these measurements for a pillar was 0.0009g. When this error was propagated through the equation for porosity, it results in the largest variation in the porosity of 0.08%. In most cases, the variation, if any, is much smaller. Since such small variation was difficult to illustrate in the plots using error bars, we have not included them in Figures 8 and 9.

Though the error in density due to the measurement process is negligible, we expect that multiple pillars built using a fixed set of process parameters will likely have slightly different densities. This could be caused by several factors, including the actual values of a process parameter being different from the value to which it is set, variation in values of the process parameters during the build process, and variation in the powder quality. Based on the results in Figures 8 and 9, we expect that this variation will likely be larger at the lower power values, but smaller at higher power values.

The porosity determined by the volumetric fraction method using SEM (Section 3.1.2) for the subset of 8 pillars built using LPW powder is listed in Table 4, along with the porosity obtained using the Archimedes method. The results indicate that either the Archimedes method overestimates the porosity or that the material is too inhomogeneously porous that one section using the microscopy technique is not valid.

5 Conclusions

In this paper, we showed how we can exploit prior knowledge, simulations based on a simple Eagar-Tsai model, and simple single-track experiments to guide the choice of parameters for building

high-density parts using an additive manufacturing process. By suitably analyzing the data from the experiments and simulations, and combining the results with prior knowledge, we were able to create small pillars with >99% relative density for a range of power values from 150W to 400W. We expect that a similar approach could be used for obtaining the process parameters that optimize other properties of the manufactured part.

Our analysis of the simulations using the Eagar-Tsai model also indicated that, for the design space explored in our analysis, the laser speed and power were the most important process parameters among the ones used as input to the simulations. Such analysis techniques would enable us to focus on a few important variables in designing our physical experiments, thus reducing the number of iterations to obtain optimal processing parameters. Though our model was a simple one, its simplicity made it computationally efficient, enabling us to sample the design space adequately. These initial sample points in feasible regions could be used as inputs to more complex models, providing further insights that could be exploited prior to the identification of process parameters.

Our physical experiments also provided some insights into the manufacturing of high-density parts. First, as expected, we found that for a given power value, increasing the speed leads to insufficient melting and lower density. We also found that the density reduces if the speed is too low, due to voids created as a result of keyhole mode laser melting; this reduction in density is however not as large as that resulting from insufficient melting. Second, we found that the use of different powders affected densities at lower power, but not at higher power. Finally, we found that at higher powers, the density is high over a wider range of scan speeds, unlike at lower powers. This would indicate that higher powers could provide greater flexibility in choosing process parameters that optimize various properties of a manufactured part. However, it remains to be seen if the operation at higher powers will have other negative effects on the micro-structure or mechanical properties of a part.

6   Acknowledgements

References

Buchbinder, D., Schleifenbaum, H., Heidrich, S., Meiners, W., and Bültmann, J. (2011). High Power Selective Laser Melting (HP SLM) of Aluminum Parts . *Physics Procedia 12, Part A*, 12:271–278.

Dadbakhsh, S., Hao, L., and Sewell, N. (2012). Effect of selective laser melting layout on the quality of stainless steel parts. *Rapid Prototyping Journal*, 18:241–249.

Delgado, J., Ciurana, J., and Rodriguez, C. (2012). Influence of process parameters on part quality and mechanical properties for DMLS and SLM with iron-based materials . *Int. J. Adv. Manuf. Technol.*, 60:601–610.

Fang, K.-T., Li, R., and Sudjianto, A. (2005). *Design and Modeling for Computer Experiments.* Chapman and Hall/CRC Press, Boca Raton, FL.

Inselberg, A. (2009). *Parallel Coordinates: Visual Multidimensional Geometry and Its Applications.* Springer, New York, NY.

Kamath, C. (2009). *Scientific Data Mining: A Practical Perspective.* Society for Industrial and Applied Mathematics (SIAM).

Kruth, J., Badrossamay, M., Yasa, E., Deckers, J., Thijs, L., and Van Humbeeck, J. (2010a). Part and material properties in selective laser melting of metals. In *Proc. 16th International Symposium on Electromachining (ISEM XVI), Shanghai, China.*

Kruth, J.-P., Deckers, J., Yasa, E., and Wauthlé, R. (2010b). Assessing influencing factors of residual stresses in selective laser melting using a novel analysis method. In *Proc. 16th International Symposium on Electromachining (ISEM XVI), Shanghai, China*, pages 531–537.

Laohaprapanon, A., Jeamwatthanachai, P., Wongcumchang, M., Chantarapanich, N., Chantaweroad, S., Sitthiseripratip, K., and Wisutmethangoon, S. (2012). Optimal scanning condition of selective laser melting processing with stainless steel 316l powder. *Material and Manufacturing Technology Ii, Pts 1 and 2. Trans Tech Publications Ltd, Stafa-Zurich*, pages 816–820.

Liu, B., Wildman, R., Tuck, C., Ashcroft, I., and Hague, R. (2011). Investigation the effect of particle size distribution on processing parameters optimisation in selective laser melting process. In *International Solid Freeform Fabrication Symposium: An Additive Manufacturing Conference, D. Bourell (Ed.), University of Texas at Austin, Austin, Texas*, pages 227–238.

Madison, J. and Aagesen, L. (2012). Quantitative characterization of porosity in laser welds of stainless steel. *Scr. Mater.*, 67:783–786.

Niendorf, T., Leuders, S., Riemer, A., Richard, H., Troster, T., and Schwarze, D. (2013). Highly anisotropic steel processed by selective laser melting. *Metall. Mater. Trans. B-Proc. Metall. Mater. Proc. Sci.*, 44:794–796.

Oehlert, G. W. (2000). *A First Course in Design and Analysis of Experiments.* W. H. Freeman. Available from http://users.stat.umn.edu/~gary/Book.html.

Rai, R., Elmer, J., Palmer, T., and DebRoy, T. (2007). Heat transfer and fluid flow during keyhole mode laser welding of tantalum Ti-6Al-4V, 304L stainless steel and vanadium . *Journal of Physics D-Applied Physics*, 40:5753–5766.

Sisto, A. and Kamath, C. (2013). Ensemble feature selection on scientific data analysis. Technical Report LLNL-TR-644160, Lawrence Livermore National Laboratory.

Spierings, A. and Levy, G. (2009). Comparison of density of stainless steel 316L parts produced with selective laser melting using different powder grades . In *Twentieth Annual International Solid Freeform Fabrication Symposium An Additive Manufacturing Conference, D. Bourell (Ed.), University of Texas at Austin, Austin, Texas*, pages 342–353.

Yadroitsev, I. (2009). *Selective laser melting : direct manufacturing of 3D-objects by selective laser melting of metal powders.* LAP Lambert Academic Publishing.

Yadroitsev, I., Gusarov, A., Yadroitsava, I., and Smurov, I. (2010). Single track formation in selective laser melting of metal powders. *Journal of Materials Processing Technology*, 210:1624–1631.

Yadroitsev, I. and Smurov, I. (2010). Selective laser melting technology: from the single laser melted track stability to 3d parts of complex shape. *Physics Procedia*, 5:551–560.

Yasa, E. (2011). *Manufacturing by Combining Selective Laser Melting and Selective Laser Erosion / Laser Re- Melting.* PhD thesis, Faculty of Engineering, Department of Mechanical Engineering. Katholieke Universiteit Leuven, Heverlee (Leuven).

Yasa, E., Craeghs, T., Badrossamay, M., and Kruth, J.-P. (2009). Rapid Manufacturing Research at the Catholic University of Leuven. In *RapidTech 2009: US-TURKEY Workshop on Rapid Technologies, Istanbul, Turkey.*

Yasa, E., Deckers, J., and Kruth, J. (2011). The investigation of the influence of laser re-melting on density, surface quality and microstructure of selective laser melting parts. *Rapid Prototyping Journal*, 17:312–327.

Yasa, E., Deckers, J., Kruth, J., Rombouts, M., and Luyten, J. (2010). Investigation of sectoral scanning in selective laser melting. In *Proceedings of the ASME 10th Biennial Conference on Engineering Systems Design and Analysis, Vol 4*, pages 695–703.